

Multiwalled Carbon Nanotubes Decorated with $\text{Mn}_{0.5}\text{Zn}_{0.5}\text{Fe}_2\text{O}_4$ Nanoparticles for Magneto-Photothermal Cancer Therapy

Kaiming Shen, Yunfei Yan,* Zongguo Xue, Shuo Wu, Jingxiang You, Lixian Li,* and Wen Siang Lew*

Cite This: *ACS Appl. Nano Mater.* 2023, 6, 13330–13341

Read Online

ACCESS |

Metrics & More

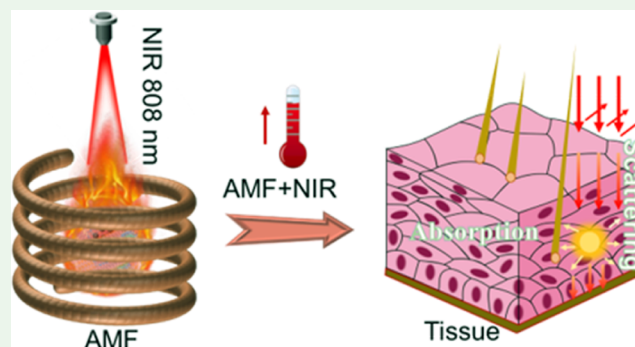
Article Recommendations

Supporting Information

ABSTRACT: Alternative cancer treatments such as photothermal therapy (PTT) and magnetic hyperthermia (MHT) techniques have been studied to show promising potential as supplementary modalities. However, such techniques have their own limitations; for instance, highly concentrated intratumoral injections of magnetic nanoparticles are required to compensate their low specific loss power under safe and low magnetic field intensity for the MHT, while the PTT has limitations in the treatment of deep-seated tumors due to low light penetration. Here, the decoration of the multi-walled carbon nanotube (MWCNT) surface by magnetic nanoparticles (≈ 8.5 nm) was achieved by a hydrothermal method and the development of MWCNT/ $\text{Mn}_{0.5}\text{Zn}_{0.5}\text{Fe}_2\text{O}_4$ (MZFC) hybrids for magneto-photothermal dual-mode cancer therapy.

The obtained specific loss power of the MZFC hybrids is found to be at least 1 order of magnitude higher, with improvement from ~ 19 W/g to 225 W/g, under the excitation of both an AMF with a magnetic field intensity of 6.4 kA/m and a frequency of 300 kHz and a simultaneous NIR laser of 0.5 W/cm² irradiation. The synergistic utilization of the photothermal and magnetic properties of MZFC effectively diminishes the required magnetic field amplitude and NIR laser power density. Our in vitro cell experiments confirmed that the thermal effects mediated by the MZFC after endocytosis delivered enhanced cytotoxicity in the presence of dual excitation of NIR laser and AMF. These findings indicate that MZFC nano hybrids possess significant potential as targeted nanoheating agents for hyperthermia applications.

KEYWORDS: functional nano hybrids, photothermal therapy, magnetic hyperthermia, magneto-photothermal, synergistic therapy



1. INTRODUCTION

Progress in the research of tumor nanotherapy has been encouraging over the past decades. Nanoparticles with unique multifunctional features for combinative cancer therapy have been extensively developed, which is considered an emerging approach in nanomedicine. Specifically, the use of energy-absorbing thermosterapeutic metals (gold, silver)^{1–8} and magnetic nanoparticles (MNPs)^{9–14} has rapidly making progress in cancer treatment technology, *i.e.*, photothermal or magnetic hyperthermia.^{12,15–17} The merits of this therapeutic modality originate from the unique multifunctional features, which play a significant role in controlling local heating inside the cells. This modality increases the hyperthermia therapy efficiency and accuracy while reducing the side effects and invasiveness by keeping the temperature of healthy tissue at the physiological level via remote-controlled heat mediators.¹⁸ Two types of hyperthermia depending on the stimulus used as a trigger, *i.e.*, optical or magnetic properties activated nanoheating agents. Magnetic hyperthermia (MHT) utilizes heat dissipation by MNPs to kill tumor cells when under an alternating magnetic field (AMF),^{19–22} while photothermal therapy (PTT) employs photothermal agents that are activated

by near-infrared laser (NIR) irradiation.^{23–27} However, both magnetic hyperthermia and photothermal therapy have their limitations.^{28,29} For instance, highly concentrated intratumoral injections of magnetic nanoparticles are required to compensate the low specific loss power (SLP) under low magnetic field intensity for the MHT,³⁰ the real-time temperature monitoring is invasive thermometry,³¹ and the nanoparticles distribute non-uniformly within the tumor.³² Therefore, enhancing SLP value through modifications in the material properties, size, shape, and aggregation state of magnetic nanoparticles emerges as the pivotal factor for augmenting the effectiveness of magnetic hyperthermia.^{33–36} In PTT, high-power laser exposure can damage surrounding healthy tissue, and some nanoparticles (gold and silver) used are not FDA-approved materials and may not meet biosafety requirements.³⁷

Received: May 7, 2023

Accepted: July 4, 2023

Published: July 13, 2023



Moreover, the photothermal therapy has long been limited to superficial tumors; in the best scenario, near-infrared light in the second region can penetrate breast tissue for 10 cm and skull/brain tissue or deep muscle for 4 cm. However, due to tissue absorption and light scattering, the photothermal effect is markedly weakened for the case of deep tumors.^{38–40} Therefore, there have been initiatives to search for more effective hyperthermia therapy approach by consolidating different modulates.^{41–44} An effective strategy involves the synergistic combination of magnetic hyperthermia (MHT) and photothermal therapy (PTT) to generate cumulative heating at a specific site of interest. In addition to the cumulative effect, this combined approach leverages the complementarity of PTT and MHT, leading to a synergistic hyperthermia effect. An advantageous characteristic of magnetic hyperthermia (MHT) is its ability to be performed without limitations related to tissue depth. Furthermore, the iron oxide nanoparticles have obtained approval as contrast agents for magnetic resonance imaging (MRI), which can realize the integration of tumor diagnosis and treatment.^{45,46} Nevertheless, MHT produces a significantly lower heating yield per unit mass compared to PTT.

Combining PTT and MHT implies providing nanohybrids with responsiveness simultaneously to both AMF and NIR to overcome their intrinsic limitations. Consequently, reduced nanoparticle injected dose and NIR laser power exposure may be achieved by combination therapy. Moreover, Multifunctional nanohybrids exhibit image trackability through different modalities. The magnetic component can be visualized using MRI, while the light-absorbing part can be imaged through photoacoustic imaging.

To date, significant efforts have been made to construct multifunctional nanohybrids as a platform for synergistic therapy.^{47,48} For instance, Curcio et al.¹⁵ reported that the use of dual heating capability (PTT + MHT) in synthesized iron oxide nanoflowers @ CuS Hybrids reduced nanoparticle administered dose, magnetic field frequency, and laser power exposure. Numerous studies about gold or silver plasmonic nanostructures have been explored for combining PTT + MHT. Srikanth et al.³⁷ designed multifunctional Ag/Fe₃O₄ nanoflowers to act as dual hyperthermia agents, and their results showed that the specific absorption rate of Ag/Fe₃O₄ nanoflowers was increased significantly under simultaneous AMF and NIR laser irradiation. Fiorito et al.⁴⁹ successfully synthesized multifunctional three-material inorganic heterostructures (Fe₃O₄@Au@Cu_{2-x}S) as an effective route for enhancing their heating ability; the presence of Au and Cu_{2-x}S domains enables substantial adsorption in the first near-infrared (NIR) biological window. Combining MHT and PTT can be selected for a more efficient treatment. Recently, although based on Fe₃O₄ nanohybrids, they have been intensively investigated, as mentioned above. However, The Curie temperature of Fe₃O₄, which is 858 K, exceeds the desirable range (315–320 K) for efficient heat generation purposes.⁵⁰ Previous reports indicate that Mn–Zn ferrite exhibits a low Curie temperature and that its magnetic properties can be modulated via introducing a minor concentration of Zn through doping.^{51,52} Additionally, manganese zinc-ferrite with good biocompatibility⁵³ and magneto-photothermal properties provided as a competitive nanoheater in clinical conditions. Functionally modified zinc–manganese ferrite can yield unexpected properties. For instance, MnZnFe₂O₄ @ starch nanoparticles exhibits good

colloidal stability, dispersibility, and the heating efficiency.⁵¹ Zn_xMn_{1-x}Fe₂O₄@SiO₂:zNd³⁺ core–shell nanoparticles show a good synergistic heating effects under simultaneous exposure with an alternative magnetic field and NIR laser.⁵⁴ Additionally, studies demonstrated that graphene, carbon nanotubes, or organic substances such as polypyrrole and polythiophene have good biocompatibility, and high photothermal conversion efficiency under NIR. Moreover, graphene and carbon nanotubes have excellent thermal conductivity, which can dramatically increase the thermal conductivity of the hybrid doping carbon nanotubes. As a result, the hyperthermia efficiency and temperature distribution will be significantly improved under the excitation of an AMF or NIR laser.^{15,48} For example, Wang et al.⁵⁵ constructed multiscale graphene aerogel polymer composites that exhibit high-efficiency heating capability and temperature stability for hyperthermia applications. An eco-friendly magnetic graphene oxide–lignin nanocomposite was fabricated, which can achieve considerable performance under the AMF in fluid hyperthermia therapy.⁵⁶ Magnetic carbon nanotubes with low Curie temperatures were proposed by Zuo et al. for self-regulating the temperature of magnetic hyperthermia.⁵⁷ Carbon nanotubes (CNTs) can engage in non-covalent and covalent π – π interactions with molecules through their surfaces of CNTs. Functionalizing the surface of CNTs with hydrophilic atoms can address the issue of aggregation. Additionally, hydrogen bonding interactions have been demonstrated to be effective in modulating the properties of pharmaceutical compounds and in applications such as drug evaluation, identification, and delivery.⁵⁸ Despite the remarkable efforts primarily focused on exploring the photothermal and magnetic hyperthermia properties of magnetic composites, less attention has been paid to developing their synergetic properties for hyperthermia therapy applications. However, a combination of the two modes can offer several advantages over using either approach alone, including complementary mechanisms, synergistic effects, versatility, and non-invasiveness.

We synthesized a nanocomposite that can produce dual-thermal effects to achieve enhanced heating efficiency for magneto-photothermal cancer therapy applications. The nanohybrids composed of Mn_{0.5}Zn_{0.5}Fe₂O₄ and MWCNTs, which demonstrated simultaneous stimulation of MWCNTs/Mn_{0.5}Zn_{0.5}Fe₂O₄ (MZFC) hybrids with a low iron concentration, can provide unrivaled heating efficiency at a clinically compatible dose of acceptable irradiation. This dual heating effect was evaluated across a range of biological complexities, starting from aqueous suspensions to in vitro tumor cells. In all tested scenarios, both heating effects demonstrated significant efficacy. While each heating modality alone was moderately cytotoxic, impairing the viability of some cancer cells, the combination of magnetothermal therapy and photothermal therapy achieved complete cancer cell death.

2. EXPERIMENTAL SECTION

2.1. Synthesis Procedure. MWCNTs/Mn_{0.5}Zn_{0.5}Fe₂O₄ nanohybrids were synthesized using the solvothermal/polyol method. A typical reaction was performed as follows: 2.7 g of FeCl₃·6H₂O, 0.495 g of MnCl₂·4H₂O, and 0.34 g of ZnCl₂ were dissolved in 70 mL of diethylene glycol (DEG) at 90 °C, and certain carboxylated multiwalled carbon nanotubes (MWCNTs) were added into the solution and stirred under room temperature to form a precursor solution. Meanwhile, 1 g of flaky sodium hydroxide (NaOH) was dissolved in DEG (20 mL) at 90 °C, followed by adding the NaOH solution and 30 mL of diethanolamine (DEA) into the precursor

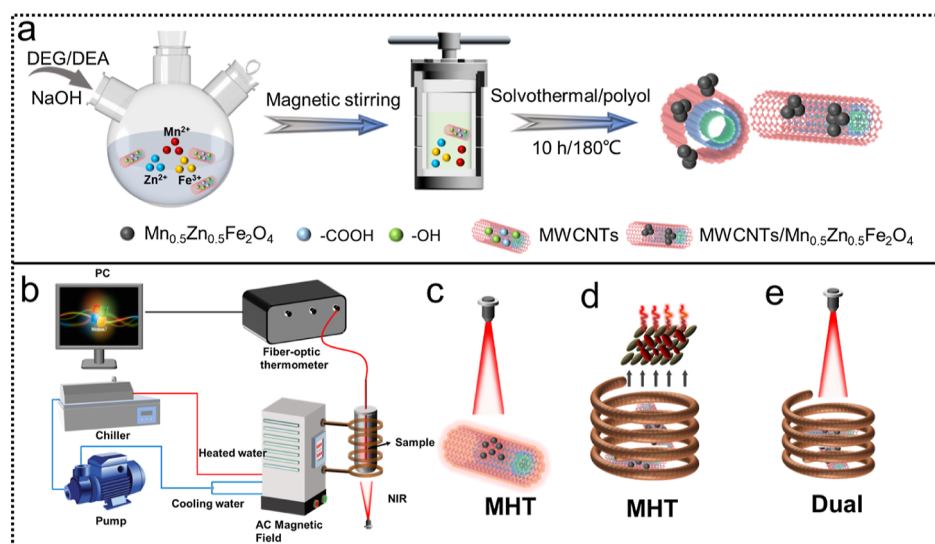


Figure 1. (a) Illustration of the synthesis process of MWCNTs/ $\text{Mn}_{0.5}\text{Zn}_{0.5}\text{Fe}_2\text{O}_4$ hybrids. (b) Schematic of measurement setup of MWCNTs/ $\text{Mn}_{0.5}\text{Zn}_{0.5}\text{Fe}_2\text{O}_4$ hybrids for magnetic hyperthermia, photothermal hyperthermia, and dual magneto-photothermal applications. Enlarged diagram of the apparatus for magnetic hyperthermia (c), photothermal hyperthermia (d), and the dual (e) in vitro application.

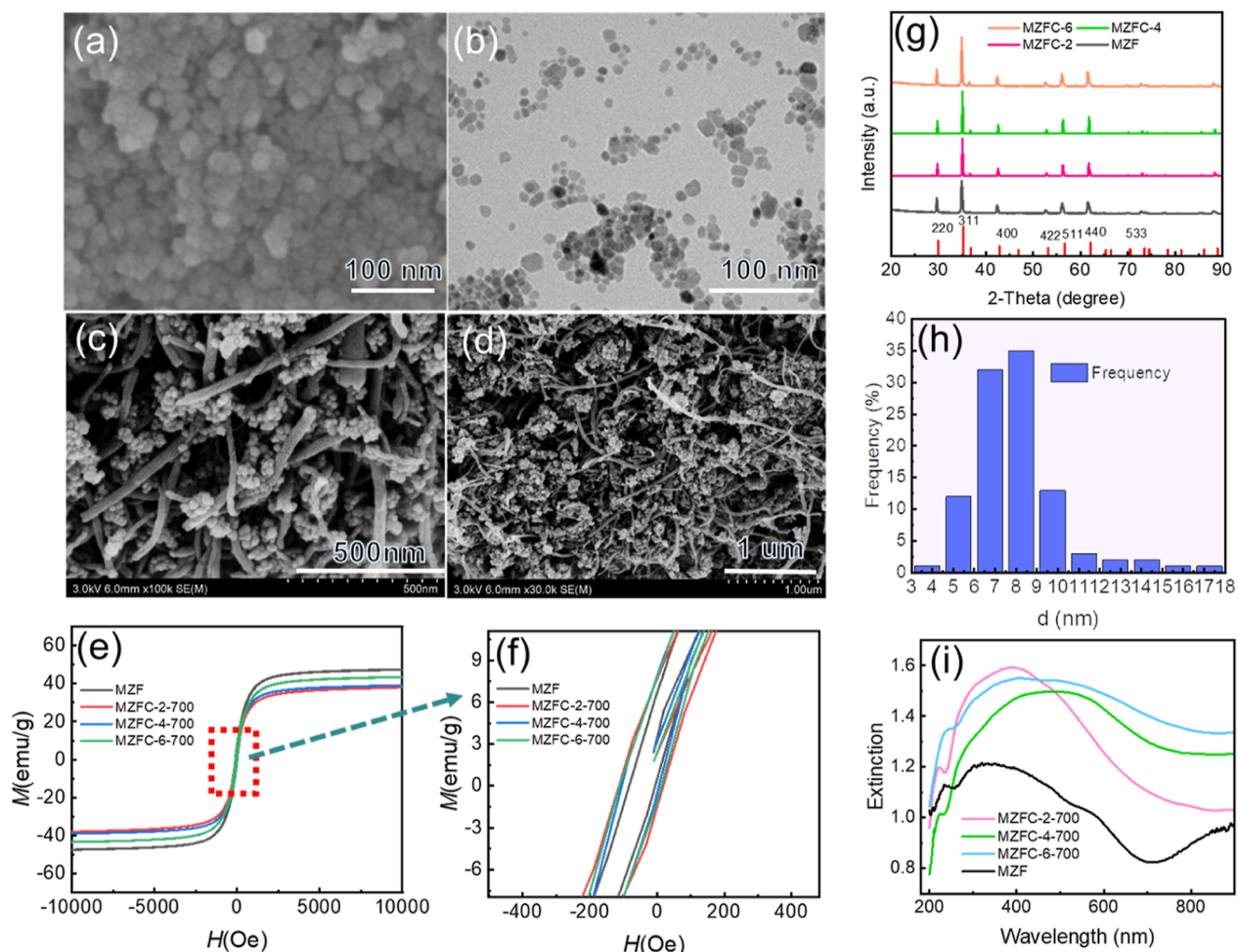


Figure 2. (a) SEM image of $\text{Mn}_{0.5}\text{Zn}_{0.5}\text{Fe}_2\text{O}_4$ nanoparticles. (b) TEM image of $\text{Mn}_{0.5}\text{Zn}_{0.5}\text{Fe}_2\text{O}_4$ nanoparticles. (c,d) SEM image of MZFC-4 hybrids in different magnifications. (e) M-H measurements of MWCNTs/ $\text{Mn}_{0.5}\text{Zn}_{0.5}\text{Fe}_2\text{O}_4$ synthesized with different contents of MWCNTs. (f) Enlarged M-H measurement at low fields for determination of M and H values. (g) XRD measurements of MWCNTs/ $\text{Mn}_{0.5}\text{Zn}_{0.5}\text{Fe}_2\text{O}_4$ hybrids with different contents of MWCNTs. (h) Size distribution of the MZFC-4. (i) Typical extinction spectrum of the MWCNTs/ $\text{Mn}_{0.5}\text{Zn}_{0.5}\text{Fe}_2\text{O}_4$ dispersed in water.

solution and stirred vigorously for 15 min to form a homogeneous solution. The solvothermal synthesis was carried out in a 200 mL autoclave for 10 h at 180 °C. Finally, the product was magnetically separated, and then particles were rinsed with alcohol and deionized water until there were no unreacted floaters on the top of the liquid before overnight drying at 60 °C.

For comparison purposes, the $\text{Mn}_{0.5}\text{Zn}_{0.5}\text{Fe}_2\text{O}_4$ (MZFC) nanoparticles were synthesized using the same method but without the addition of carboxylic MWCNTs. The synthesized samples were labeled as MZFC- n ($n = 1, 2, 4, 6,$ and 8) according to the different mass percentage contents of MWCNTs. The preparation route of MZFC- n is displayed in Figure 1a.

2.2. Magnetic Hyperthermia Measurement. MWCNTs/ $\text{Mn}_{0.5}\text{Zn}_{0.5}\text{Fe}_2\text{O}_4$ (1 mg) were dispersed in deionized water (1 mL). The magnetic hyperthermia efficiency was studied using a calorimetric method. The MZFC was dispersed in the gel phantom with a cylindrical hole and then exposed in the AMF with a $f = 300$ kHz and $H = 6.4$ kA/m to 7.2 kA/m. The temperature rise was recorded with a probe of a fiber-optic temperature converter. A real-time infrared thermal imaging camera was also used for monitoring. The description of the gel phantom fabrication is in the Supporting Information section. In order to minimize thermal fluctuations, the temperature within the coil was maintained at 27 °C using a water cooling circuit. The temperature increase was measured over time (dT/dt) during the initial linear slope ($t \approx 30$ s) to assess the heating effect in relation to SLP, which is defined as the power dissipation per unit mass of sample (W/g)

$$\text{SLP} = \frac{C V_s dT}{m dt}$$

where C is the specific heat capacity of the sample, m is the total mass of the sample, and V_s is the volume of the sample.

2.3. Photothermal and Dual Magneto-Photothermal Measurements. Photothermal experiments were conducted under the NIR (808 nm) with a constant power density (0.5, 1 W/cm²) irradiation. The aqueous suspension of nanoparticles, enclosed within a 5 mL EP tube, was subjected to illumination by an NIR laser positioned at a distance of 5 cm from the sample. The laser power densities of 0.5 and 1 W/cm² for the respective applied powers. During the study on photothermal conversion efficiency, the MZFC-4 dispersion exhibited an optical extinction of 1.3 at 808 nm. In the photothermal conversion efficiency study, the optical extinction at 808 nm for the MZFC-4 dispersion was adjusted to 1.3. Schematic of the photothermal and magnetic hyperthermia experimental setup is shown in Figure S4a,b.

2.4. Cellular Uptake. To conduct cellular uptake experiments, we synthesized MZFC incorporating IR780 using a previously established method,⁵⁹ where IR780, a prototypic NIR heptamethine cyanine agent, was loaded into MZFC-4. This agent emits fluorescence with high intensity within the 807–823 nm wavelength range, making it suitable for imaging applications. The MCF-7 cells were incubated in a confocal Petri dish (with a diameter of 20 mm) at a density of 2×10^5 cells per well and cultured for 12 h. The cells were then incubated with MZFC-4/IR780 (IR780 with a concentration of 10 μM) at 37 °C for 2 h. After three washes, the cells were subjected to staining with LysoBrite Green (1 μM) and Hoechst 33342 (10 $\mu\text{g}/\text{mL}$) at 37 °C for 20 min. Following another three washes with PBS, the cells were visualized using a confocal microscope.

2.5. In Vitro Viability Assays of MZFC. The MCF-7 cells were utilized to evaluate the biocompatibility of MZFC. Initially, the cells were seeded onto a 96-well plate (1×10^4 cells/well). Then a 24 h incubation period to allow cell adhesion, the media were removed, and then washed with PBS. Then the cells were incubated with varying concentrations (0–1000 $\mu\text{g}/\text{mL}$) of MZFC. Following an additional incubation period of 24 h and 48 h for different control groups, the culture medium was substituted with DMEM and using MTT to assay cell viability.

2.6. Evaluation of Toxicity. MCF-7 cells were plated in laser-confocal Petri dishes (2×10^5 cells/well) and cultured for a duration of 24 h. Following multiple washes with PBS and replacement with

fresh DMEM, the MCF-7 cells were plated with varying concentrations of MZFC-4 and incubated for a duration of 4 h. Subsequently, the cells were subjected to irradiation using both an AMF ($H = 6.7$ kA/m, $f = 300$ kHz) and an NIR ($P = 0.5$ W/cm²) for 10 min. The cells were treated using magneto-photothermal for 10 min, subsequently incubated with DMEM for 20 min. The calcein-AM and propidium iodide (PI) staining was performed, and imaging using a fluorescent inverted microscope. Furthermore, cell viability following the dual-mode treatment was assessed using an MTT assay.

3. RESULTS AND DISCUSSION

3.1. Structural Characterization. The as-prepared MZFC and MZFC-4 samples underwent characterization using SEM and TEM, and the corresponding images are depicted in Figure 2a–d. The SEM images of MZFC-2 and MZFC-6 can be found in Figure S1a–c. Notably, the SEM images revealed the interweaving of a network of MWCNTs among the $\text{Mn}_{0.5}\text{Zn}_{0.5}\text{Fe}_2\text{O}_4$ grains (Figure 2c,d). Additionally, Figure 2h displays $\text{Mn}_{0.5}\text{Zn}_{0.5}\text{Fe}_2\text{O}_4$ nanoparticles randomly dispersed on the MWCNTs, showcasing an average diameter of approximately 8.5 nm. The observed distribution can be attributed to the carboxyl groups present on MWCNTs. The DLS results of as-prepared samples indicated the formation of MZFC-4 with an average size of 6.5 nm, as shown in Figure S2.

The prepared MZFC nanohybrids were characterized using X-ray diffraction (XRD). As depicted in Figure 2g, the diffraction patterns revealed distinct peaks corresponding to crystallographic planes. These peaks can be attributed to the spinel structure of $\text{Mn}_{0.5}\text{Zn}_{0.5}\text{Fe}_2\text{O}_4$.^{60,61} Notably, the diffraction peak associated with the multi-walled carbon nanotubes (MWCNTs) was not observed, suggesting a low concentration of MWCNTs in the nanohybrids. Furthermore, no peaks indicative of crystalline impurities were detected, affirming the synthesis of high-purity Mn–Zn ferrite with good crystallinity.^{51,62}

The FTIR spectra of MZFC nanohybrids were obtained and are presented in Figure S1d. The band observed at 3422 cm⁻¹ can be owed to the O–H stretching mode, which corresponds to either free water or water molecules adsorbed onto the samples. The peaks observed at 682 and 1739 cm⁻¹ arise from the bending vibrations of the C–H bonds and the bending absorption of the COO⁻, respectively. Moreover, the peak detected at 1739 cm⁻¹ corresponds to the stretching vibration of C=O, indicative of carbonyl or carboxylic acid moieties. The bands observed in 900–1200 cm⁻¹ due to the C–O–C and C–O bonds stretching vibration. Additionally, the absorption peak at 1627 cm⁻¹ is indicative of the unoxidized MWCNT domains skeletal vibration, suggesting the existence of a sp² hybridized honeycomb lattice structure. Finally, the band in the range of 540–560 cm⁻¹ is assigned to the stretching vibrations of the octahedral M–O bonds and tetrahedral in the ferrite structure. The UV–vis–NIR spectra of MZFC- n aqueous dispersions at concentrations of 0.5 mg/mL are shown in Figure 2i. It is noteworthy that the samples displayed broadband extinction across the visible to near-infrared light range at varying contents of multi-walled carbon nanotubes (MWCNTs). Notably, the doped carbon nanotubes exhibited considerably higher light absorption compared to their undoped counterparts, implying the potential for enhanced photothermal effects in the doped samples. Particularly for MZFC-4, an extinction of approximately 1.3 was observed at a wavelength of 808 nm, which serves as a critical parameter for calculating the photothermal conversion efficiency.

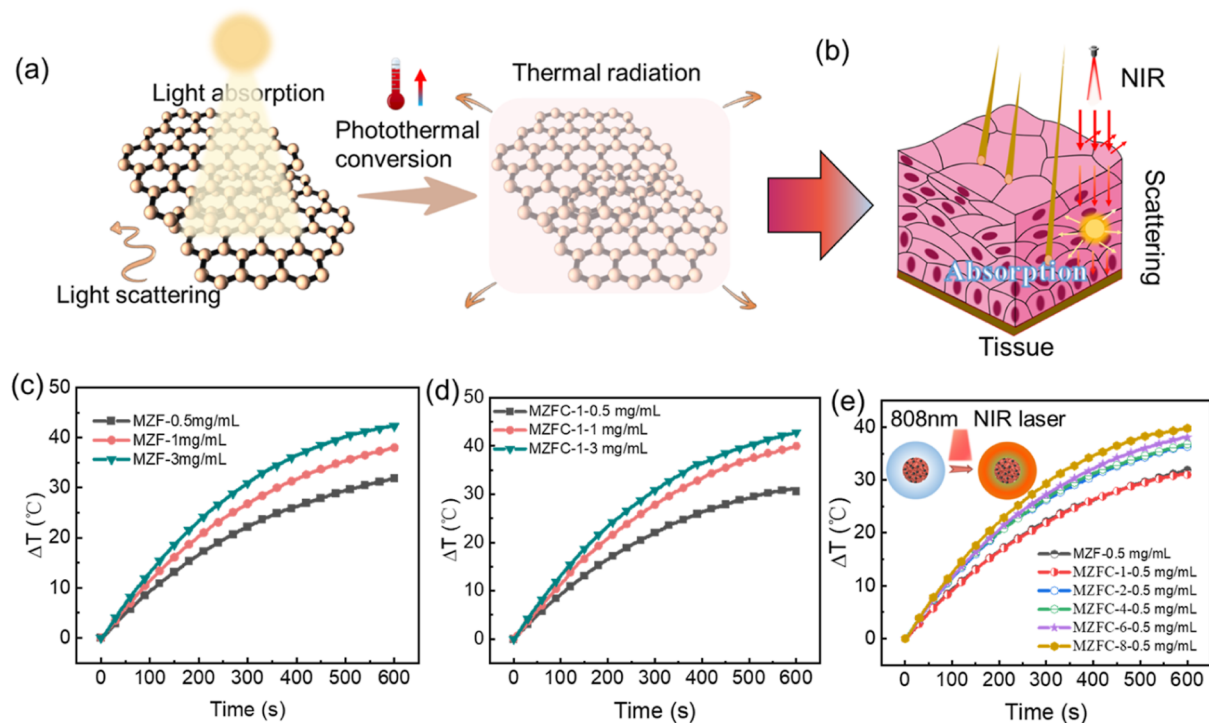


Figure 3. (a) Schematic diagram of photothermal conversion. (b) Scattering and absorption of near-infrared light inside the tissue. Photothermal performances of the MZFC nano hybrids in solution. Heating curves under a period of 10 min irradiation with an 808 nm laser for values of the power density of 1 W/cm^2 (c) various concentrations of MZF (d) various concentrations of MZFC-1. (e) Temperature change curves of MZF (1 mg/mL) with different contents of MWCNTs upon irradiation of the 808 nm laser at 1.0 W/cm^2 .

3.2. Magnetic Characterization. Magnetic measurement was performed by using a vibrating sample magnetometer (VSM). The magnetic properties of each sample have been compiled and are presented in Table S1. As depicted in Figure 2e, the pure $\text{Mn}_{0.5}\text{Zn}_{0.5}\text{Fe}_2\text{O}_4$ (MZF) has a M_s value of 47.5 emu/g, and the MZFC magnetization decreases with the content of MWCNTs increases. The $M-H$ loops of MZFC-2 and MZFC-4 basically coincide and have a minimum value of 39 emu/g. The presence of MWCNTs plays a diluent role, leading to a decrease in saturation magnetization. By focusing on the low-field region of the magnetic hysteresis loops, as depicted in Figure 2f, it becomes evident that all samples exhibit distinct hysteresis loops. This observation suggests the absence of a ferromagnetic state at room temperature.

3.3. Photothermal Therapy. As shown in Figure 3a, when carbon nanotubes absorb light energy, their surface electrons are excited, generating localized heat, which leads to the heating of the surrounding tumor tissue and ultimately results in the death of tumor cells. In biomedicine, the tissue has a dissipation loss of light, which hinders the effect of photothermal therapy, as schematically shown in Figure 3b. Therefore, rational selection of specific wavelengths of light and photosensitizers to enhance the photothermal conversion efficiency can effectively improve the tumor thermal ablation effect. Subsequently, photothermal conditions, such as the nanoparticles' concentration and different content of MWCNTs, were reasonably investigated as illustrated in Figure 3c, (d), and (e), and the temperature change curves of different content of MWCNTs are shown in Figure S5. Following irradiation, the solutions exhibited a rapid increase in temperature with escalating concentrations (0.5, 1, and 3 mg/mL). To ensure minimal damage to surrounding tissues and adhere to the thermal ablation temperature for cellular

death in the body ($>45 \text{ }^\circ\text{C}$), it is necessary to minimize both the concentration and laser power density employed. Ideally, a temperature change exceeding $20 \text{ }^\circ\text{C}$ is desired. Remarkably, the MZF or MZFC-1 solution (1 mg/mL) achieved a temperature rise of $30.5 \text{ }^\circ\text{C}$ when subjected to laser irradiation under a power density of 1.0 W/cm^2 . This result demonstrates the capability of satisfying the temperature requirement for tumor hyperthermia, underscoring its potential efficacy. The photothermal conversion efficiency (η_T) of the MZFC-4 nano hybrids was also calculated by following the previous method⁶³ (see SI Photothermal conversion efficiency). The nano hybrids exhibited a calculated η_T value of 41.7%, whereas the MZF alone demonstrated a value of 18.3%. This significant increase of 23.4% in the photothermal efficiency of MZFC-4 highlights the remarkable enhancement achieved by the MZFC nano hybrids in terms of their photothermal conversion ability. These findings position the MZFC nano hybrids as a promising photothermal agent with outstanding potential for various applications.

Furthermore, the effect of MZFC nano hybrids with varying contents of MWCNTs was examined under NIR laser irradiation at a power density of 1.0 W/cm^2 . The results demonstrate that photothermal therapy (PTT) mediated by MZF exhibits comparable efficacy to that of MZFC nano hybrids, but only when the MWCNT content is low. With the increase of MWCNTs, the solution temperature keeps increasing; however, it is worth noting that the temperature difference between MZF and MZF-1 is very small, and their temperature curves basically coincide. This is mainly attributable to the fact that the molar extinction coefficient of the composite does not change significantly when the doping content of MWCNTs is 1%, resulting in no improvement in the photothermal conversion effect of the

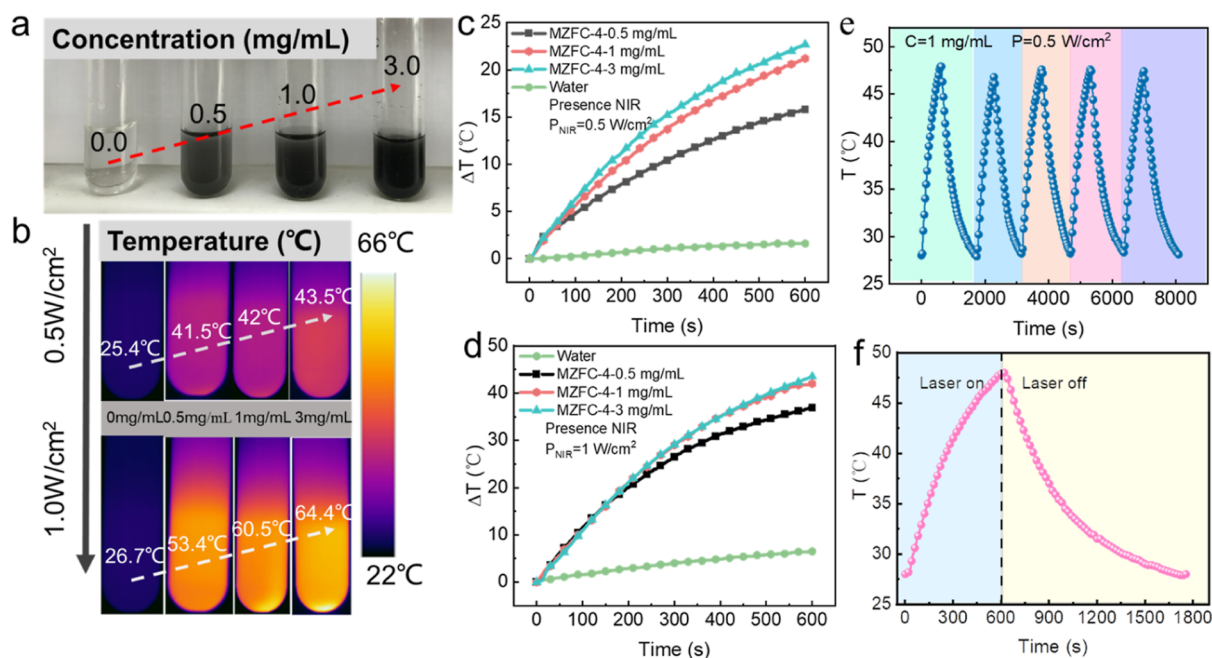


Figure 4. (a) Diagram of MZFC-4 suspension at different concentrations. (b) Infrared thermal images of MZFC-4 with various concentrations upon irradiation for 10 min. (c) Heating curves of water and MZFC-4 aqueous dispersion (0.5, 1.0, and 3 mg/mL) under the 808 nm NIR laser of 0.5, (d) 1.0 W/cm². (e) Recycle the heating–cooling curve of MZFC-4 for five on/off rounds. (f) Calculated η_T at 808 nm of MZFC-4, the curve depicts the photothermal effect of the MZFC-4 aqueous dispersion (1 mg/mL) during specific irradiation periods, followed by the cessation of laser irradiation. (The NIR laser was operated at 0.5 W/cm²).

MZFC. At the high content of MWCNTs, the heating effects of MZFC are obviously better than those of MZF. Compared with the MZF without doped MWCNTs, the temperature difference is increased by 10.2 °C when the doping content of MWCNTs is 8%. This finding holds significant implications for enhancing the efficacy of tumor hyperthermia.

3.4. Photothermal and Magnetic Thermal Properties of MWCNTs/Mn_{0.5}Zn_{0.5}Fe₂O₄ Composites. Our previous published work⁶⁴ showed that using doped carbon nanotubes can improve the magnetocaloric effect, but with the continuous increase of MWCNTs. The magnetocaloric effect exhibits an initial increasing trend followed by a significant decrease. Previous studies have shown that both MZFC-2 and MZFC-4 exhibit good magnetothermal effects.⁶⁴ Based on the findings of this paper, the photothermal conversion effect of MZFC-4 is significantly better than that of MZFC-2. Therefore, MZFC-4 was selected as the optimal sample for magnetothermal-photothermal synergistic therapy in the following experiments. The photophysical properties of MZFC were explored, including its UV absorption and photothermal conversion efficiency. Figure 4a,b demonstrates the diagram of MZFC-4 suspension and the infrared thermal images of MZFC-4 at different concentrations, respectively. Infrared thermal images of MZF with different MWCNT contents in various concentrations upon NIR laser (1 W/cm²) irradiation for 10 min are shown in Figure S6. Figure 4c illustrates the evaluation of the photothermal conversion performance of water and MZFC-4 at various concentrations under NIR laser exposure. Following a 10 min NIR laser irradiation at 0.5 W/cm², the temperature increases of water and MZFC-4 aqueous solutions at concentrations of 0.5–3 mg/mL, compared to room temperature (26.7 °C), were 1.6, 15.8, 21.2, and 22.7 °C, respectively. Upon increasing the laser power density to 1.0 W/cm², the ΔT of water and MZFC-4 aqueous solutions at the

same concentrations were 6.5, 36.9, 42, and 43.5 °C, respectively, compared to room temperature (26.7 °C). The final solution temperature gradually rose with an increase in concentration from 0 to 3 mg/mL, while the temperature change became less pronounced when the MZFC-4 concentration reached 3 mg/mL, as shown in Figure 4c. Notably, the temperature change of MZFC-4 with a concentration of 3 mg/mL closely resembled that of the 1 mg/mL concentration under a power density of 1 W/cm² (Figure 4d). Moreover, considering high doses MZFC-4 might be bio-persistent and potentially toxic, an MZFC-4 concentration of 1 mg/mL was chosen in the following experiments. The high photothermal conversion efficiency of MZFC-4 was attributed to the MWCNTs with outstanding photothermal conversion capability that did not scatter light out. Even though Mn_{0.5}Zn_{0.5}Fe₂O₄ has a poor photothermal conversion performance, doping MWCNTs significantly improved the near-infrared light absorption of nanohybrids, and as a result, the photothermal conversion efficiency was enhanced dramatically. Furthermore, MZFC-4 exhibited exceptional thermal and photostability. The photothermal conversion stability was evaluated by toggling the near-infrared (NIR) laser on and off while simultaneously recording the real-time temperature changes during the heating and cooling phases, as depicted in Figure 4e. After five cycles, the photothermal conversion capability of MZFC-4 remained consistent at a level comparable to the first cycle. Notably, there were no discernible signs of light aggregation or bleaching resulting from the temperature elevation, indicating the inherent stability of MZFC-4 against photothermal cycling. The photostability of MZFC-4 meets the requirements for PTT applications. IR thermal images of the MZFC-4 solution further demonstrated its superior photothermal therapy efficacy (Figure 4b). These results demonstrated that MZFC-

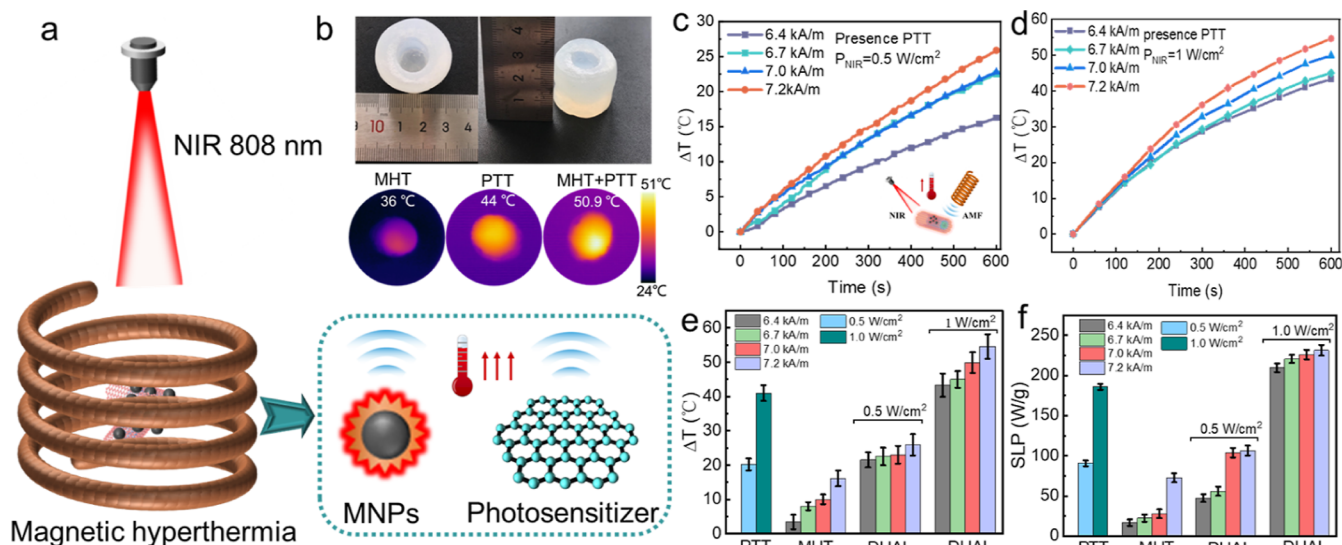


Figure 5. (a) Experimental setup for combined hyperthermia experiments is depicted schematically. (b) Gel phantom diagram and the thermal images acquired from the surface of the gel phantom (height = 3 cm and diameter = 3 cm) containing 1 mg/mL of MZFC-4 after heating 600 s for MHT, PTT, and DUAL. The heating curves of the MZFC-4 aqueous solution are presented, showcasing the response under various AC magnetic fields ($6.4 < H < 7.2$ kA/m) at $f = 300$ kHz, coupled with irradiation from an 808 nm laser at two different power densities: 0.5 W/cm^2 (c) and 1.0 W/cm^2 (d). The temperature elevation after 600 s of heating is depicted in (e), while (f) illustrates SLP as a function of H for various laser power densities.

4 is an excellent photothermal agent candidate for photothermal therapy.

The magnetothermal and photothermal effects of MZFC-4 were initially evaluated in aqueous suspensions by varying the magnetic field amplitudes within the range of 6.4–7.2 kA/m. Three heating methods were carefully selected: (i) magnetic hyperthermia only (MHT), at $f = 300$ kHz with the H from 6.4 to 7.2 kA/m; (ii) Photothermal treatment was performed solely using an 808 nm laser with power levels ranging from 0 to 1.0 W/cm^2 ; and (iii) combined MHT and PTT: simultaneous irradiation of both PTT and MHT. In order to avoid the laser probe being affected by the alternating magnetic field, the laser and the coil should be kept at a reasonable distance (5 cm), as shown in Figure 5a.

Figure 5b reveals IR images and temperature profiles in the gel phantom surface acquired with each protocol, the MZFC-4 with a concentration of 1 mg/mL. Meanwhile, the AFM with $H = 6.7$ kA/m and $f = 300$ kHz, and NIR with the $P = 0.5 \text{ W/cm}^2$. Under the MHT + PTT model, a cumulative effect was observed across all magnetic field amplitudes, and the temperature elevation caused by both PTT and MHT is more than the PTT or MHT alone (Figure 5e). In particular, it is worth noting that in the early stage of heating under the presence of NIR (1 W/cm^2), the temperature difference under each magnetic field amplitude was not obvious, mainly because the heating rate of the sample stimulated by the laser was faster than that induced by a magnetic field. However, in the late stage of heating, this phenomenon would weaken, and the sample solution under each magnetic field amplitude showed an obvious temperature difference (Figure 5d).

The magnetic and laser-induced heating can be precisely controlled by adjusting the parameters of the alternating magnetic field (AMF) and near-infrared (NIR) irradiation. The effectiveness of magnetic hyperthermia is commonly quantified by SLP, as described in the Methods Section. Consistent with expectations, the SLP exhibited an increase with both H and f of the AMF during magnetic hyperthermia

(MHT), as summarized in Figure 5f. In the MHT + PTT mode, the heating efficiency exhibited a significant increase with laser power density. Figure 5f shows the value of SLP obtained under MHT alone and in dual mode. The SLP was effectively doubled in the presence of a laser for all H , which resulted in a maximum heat generation rate of 235 W/g at an irradiation intensity of 1.0 W/cm^2 (7.2 kA/m, 300 kHz). The SLP increases at least 1 order of magnitude from the MHT (19 W/g) only to the dual mode (225 W/g). Furthermore, it is noteworthy that within the low-field range, the SLP for MZFC-4 remains relatively small. Hence, the combination of AMF and NIR laser irradiation holds even greater promise in this low magnetic field amplitude regime, rendering it more suitable for clinical trials while also yielding a more pronounced improvement in laser-induced SLP. These findings underscore the concept that developing innovative composite nanostructures with synergistic light absorption and magnetic properties for simultaneous PTT and MHT represents a crucial avenue for the advancement of highly efficient nanostructured hyperthermia agents.

To assess the heating efficiency of MZFC-4, an AMF with a strength in the range of 6.4 to 7.2 kA/m at 300 kHz was used to irradiate the MZFC-4 aqueous solution (1 mg/mL) for 10 min. Figure 6a shows the temperature profiles obtained by thermal IR for each protocol using a $H = 6.7$ kA/m at 300 kHz and a $P = 0.5 \text{ W/cm}^2$. The observed temperature increased by $28.7 \text{ }^\circ\text{C}$ for the MHT + PTT treatment for 10 min, which is comparable to the total increases under the two individual modalities, $7 \text{ }^\circ\text{C}$ for MHT only, and $22 \text{ }^\circ\text{C}$ for PTT only. The heating resulting from magnetic hyperthermia (MHT) exhibited a linear increase with the duration of alternating magnetic field (AMF) exposure, as depicted in Figure 6b. The temperature rise (ΔT) displayed a significant dependence on the magnetic field amplitude. Moreover, the temperature elevation induced by the combined approach of magnetic hyperthermia and photothermal therapy (MHT + PTT) demonstrated an augmentation with both the magnetic field

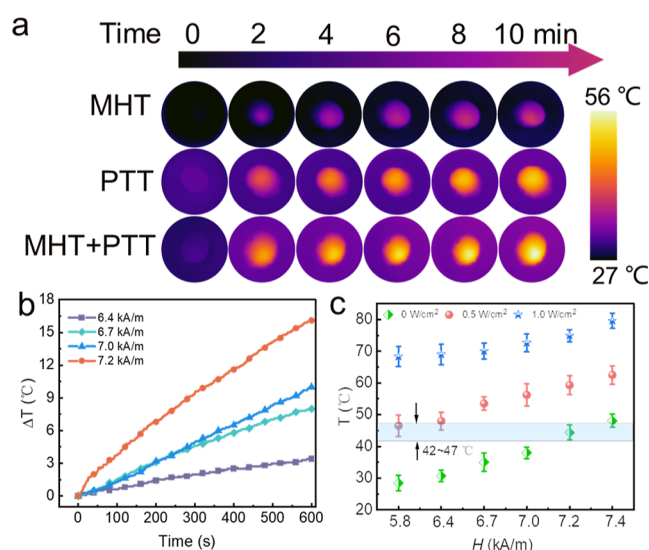


Figure 6. (a) Thermal images of MZFC-4 aqueous solution dispersed in a gel phantom, which irradiation by MHT, PTT, and DUAL for 10 min. (b) Temperature elevation of MZFC-4 solution (1 mg/mL) at different magnetic field amplitudes. (c) The achieved temperature after a 10 min heating period is plotted as a function of H for various NIR laser power densities.

amplitude (H) and laser power density, as illustrated in Figure 5c. In order to reach the targeted ablation temperature range of cellular death in the body, i.e., 42–47 °C, excitation strengths as large as $P = 1.0 \text{ W/cm}^2$ and $H = 7.2 \text{ kA/m}$ are required for individual photothermal or magnetic hyperthermia therapy, respectively. However, a major challenge in clinical trials is the need to ensure that both laser irradiation exposures and the magnetic dose are maintained below safety limits to minimize damage to healthy tissues while selectively targeting cancer cells for destruction. Simultaneous irradiation of both MHT and PTT therapies significantly lowers the required values of magnetic field amplitude (H) and laser power density (P) to achieve the desired temperature elevation within the therapeutic window, thereby enhancing the effectiveness of treatment.

The temperature elevation of the MZFC-4 solution under combined exposure to an alternating magnetic field (AMF) and an NIR laser is depicted in Figure 6c. In the absence of laser irradiation, achieving the necessary temperature range for tumor hyperthermia requires relatively high magnetic field amplitudes (H). However, in the presence of $P = 0.5 \text{ W/cm}^2$ and 1.0 W/cm^2 , a significant enhancement in the attained temperatures is observed. For instance, at $H = 5.8 \text{ kA/m}$, the temperature after 10 min of exposure increases from 29 to 46 and 67 °C for $P = 0$ and 0.5 W/cm^2 , respectively. Notably, reaching a target temperature of 42 °C without laser irradiation necessitates a $H = 7.2 \text{ kA/m}$. However, this requirement decreases considerably when simultaneous $P = 0.5$ or 1.0 W/cm^2 are applied. These findings highlight the synergistic heating effect of the MZFC-4 nanohybrids through the combined utilization of both heating modalities.

3.5. In Vitro Cell Uptake of the MZFC-4 Nanohybrids.

In the present study, cell uptake and distribution of MZFC-4 in MCF-7 cells were studied by intracellular colocalization.

The cell nuclei were stained with Hoechst, exhibiting blue fluorescence upon illumination with a 405 nm laser. While the IR780/MZFC-4 could produce red fluorescence under the

excitation of a 488 nm green laser, the lysosome was stained by LysoBrite green and could produce green fluorescence under the illumination of 500 nm. Following a 30 min, 2 h, and 4 h incubation period with MCF-7 cells, we observed strong colocalization of MZFC-4 and LysoTracker fluorescence, as depicted in Figure 7a, red fluorescence signals from MZFC-4

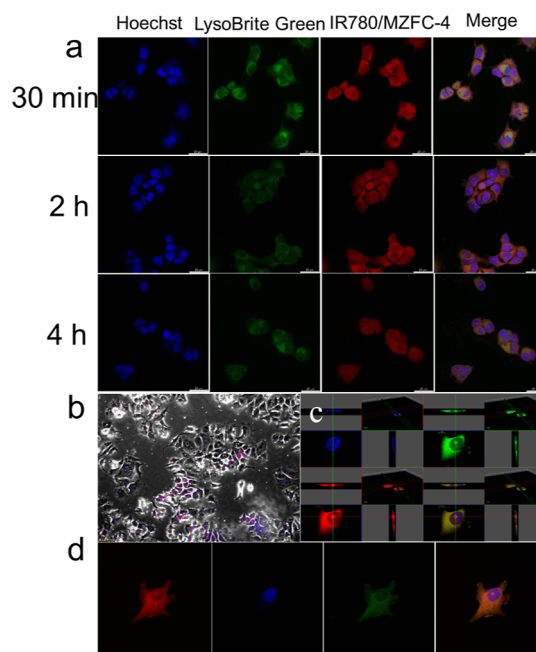


Figure 7. (a) Confocal microscope images were captured to observe the cellular uptake at 30 min, 2 h, and 4 h in MCF-7 cells incubated with MZFC-4. (b) Bright field image of cells. (c,d) Three-dimensional (3D) images were obtained to visualize the MCF-7 cells after varying incubation times with the MZFC-4 nanohybrids at a concentration of $100 \mu\text{g mL}^{-1}$.

could be observed near the lysosome, which colocalization with LysoBrite green, suggesting the endocytosis of MZFC-4-700 nanohybrids by MCF-7 cells, and the MZFC-4 was taken up via an endolysosomal pathway. Furthermore, the intracellular localization can be clearly confirmed in the 3D images as shown in Figure 7c and d. Hence, the MCF-4-700 nanohybrids demonstrated cellular internalization in tumor cells, enabling localized generation of heat through magnetic-photothermal synergistic hyperthermia therapy. Furthermore, the high specific surface area of the multi-wall carbon nanotubes allows for drug loading, such as DOX, facilitating intracellular drug delivery for chemotherapy. This property showcases significant potential for synergistic therapeutic approaches combining drug delivery, magnetic hyperthermia, and photothermal therapy.

3.6. Synergistic Effect of Magnetic-Photothermal Hyperthermia. Although the MWCNTs and MZFC nanohybrids used in this study are known to be biocompatible, it is essential to evaluate the cytotoxicity of this system to ensure its safety and suitability for biomedical applications. Therefore, further studying the biocompatibility of MZFC nanohybrids in vitro or in vivo is needed to fully realize their biomedical applications. As shown in Figure 8a,b, after incubation of MCF-7 cells with the MCF-4-7 nanohybrids for 24 and 48 h, the cell viability of the nanohybrids in the present study was found to be comparable to that of the control, even at a

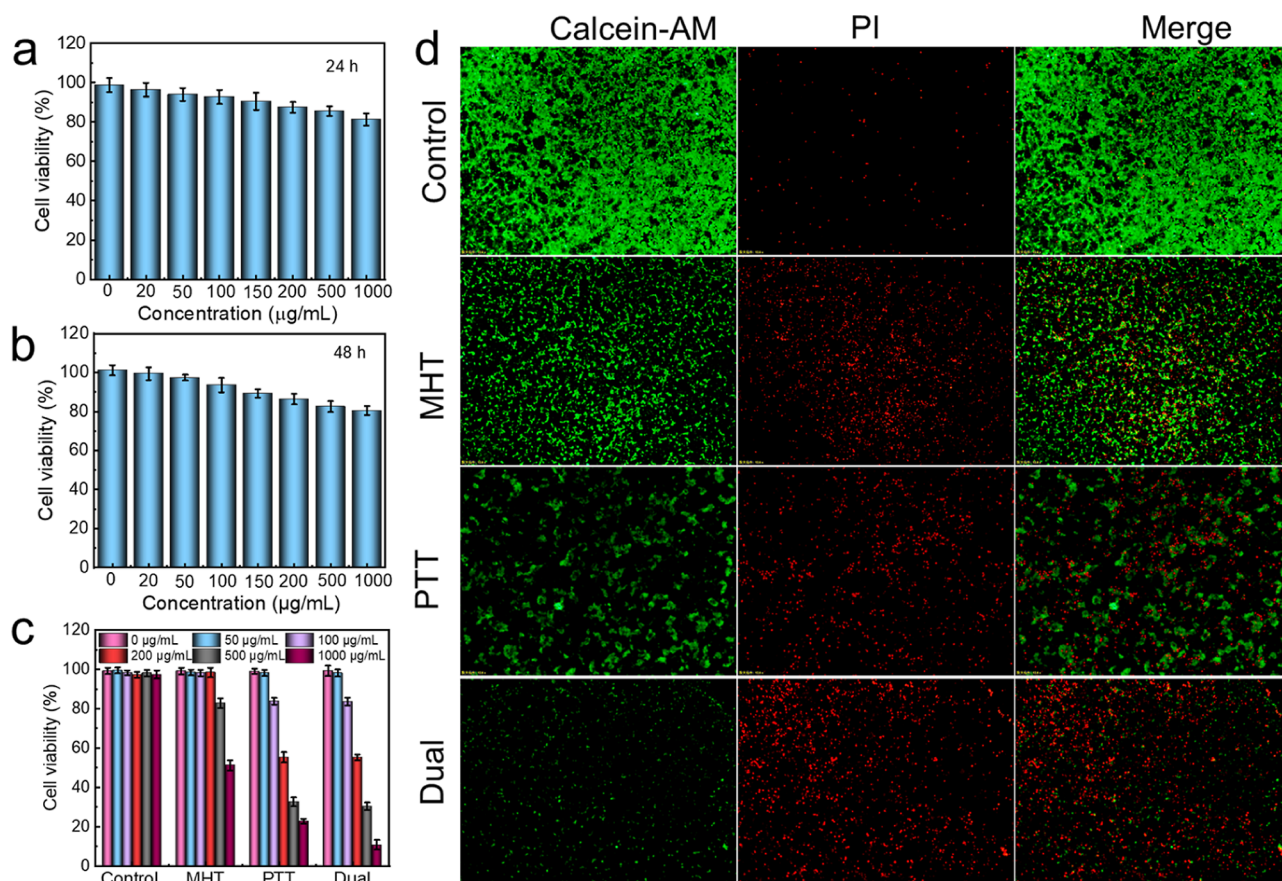


Figure 8. (a) Cell viability of cells was assessed after a 24 h incubation period with varying concentrations of MZFC-4, (b) 48 h. (c) Cell viability of MCF-7 cells was evaluated after incubation with various concentrations of MZFC-4 under alternating magnetic field exposure ($f = 300$ kHz, $H = 6.7$ kA/m) and NIR laser irradiation for 10 min. (d) Confocal images were captured to visualize the cellular staining of live cells (green fluorescence, calcein-AM) and dead cells (red fluorescence, propidium iodide) in the presence of MZFC-4 (1 mg/mL) and under the combined exposure of AMF (300 kHz, 6.4 kA/m) and NIR laser irradiation (0.5 W/cm²) for 10 min.

concentration of $1000 \mu\text{g/mL}^{-1}$. These results suggest that the nanohybrids exhibited no cytotoxicity under the tested conditions.

The cytotoxicity of MZFC-4, in combination with an AMF and N*IR laser, was assessed against MCF-7 cells using the MTT assay. As shown in Figure 8c, no significant cytotoxicity was observed on MCF-7 cells treated with a low concentration of MZFC-4 ($\sim 50 \mu\text{g mL}^{-1}$). Specifically, for MHT with high concentration dependence, the inhibitive rate of MZFC-4 was 51.4% at the concentration of 1 mg mL^{-1} under AMF (300 kHz, 6.7 kA/m) irradiation for 10 min. However, the inhibitory rate of MZFC-4 significantly increases to 71.6% when subjected to NIR laser (0.5 W/cm^2) irradiation for 10 min. This observation can be attributed to the fact that magnetic hyperthermia (MHT) generates a lower heating yield per unit mass compared to photothermal therapy (PTT). It is worth noting that the antitumor effect of MZFC-4 exhibits a concentration-dependent trend, highlighting the crucial role of MZFC-4 in hyperthermia applications. Remarkably, even in the presence of a magnetic field and NIR laser, the cell viability remains high at 97% when MCF-7 cells are incubated with MZFC-4 at a concentration below $100 \mu\text{g/mL}$. As the concentration of MZFC-4 increases, the cell viability decreases remarkably. When exposed to both NIR (0.5 W/cm^2 , 808 nm) and AMF ($f = 300$ kHz, $H = 6.7$ kA/m) irradiation, the cell viability incubated with MZFC-4 (1.0 mg L^{-1}) was 10.3%, indicating that the PTT and MHT combination augmented

the cytotoxicity of MZFC-4 remarkably. The aforementioned results confirm that the combination of MZFC-4 + dual modulation exhibits the most pronounced toxicity toward cancer cells among all the tested formulations.

The cytotoxicity data were further substantiated by the live/dead cell staining assays, providing additional evidence for the observed toxic effects of the MZFC-4 + dual modulates on cancer cells. The absence of a red fluorescence signal in the control group implies that without MZFC-4 under dual irradiation, there is no apparent cytotoxicity to cancer cells. In comparison to the control group, which only received NIR laser and AFM irradiation, the MZFC-4 group exhibited a more intense red fluorescence, confirming the cytotoxic activities of MZFC-4. Furthermore, MCF-7 cells preincubated with MZFC-4 and subsequently subjected to a combination of 808 nm laser and AMF irradiation displayed the most pronounced red fluorescence, indicating a promising synergistic effect for cancer cell eradication.

4. CONCLUSIONS

In conclusion, we have demonstrated that the heating efficiency of MZFC-4, which is a newly synthesized photo-responsive and magnetically responsive nanohybrid, is significantly enhanced by combining the magnetic hyperthermal effect of $\text{Mn}_{0.5}\text{Zn}_{0.5}\text{Fe}_2\text{O}_4$ and the photothermal response of MWCNTs. The combined PTT and MHT

techniques provide cumulative heating, hence enabled a reduced dosage. The SLP of the MZFC-4 hybrid increases by an order of magnitude under low magnetic field and simultaneous NIR laser irradiation. Due to its efficient intracellular uptake and high biocompatibility toward MCF-7 cancer cells, MZFC-4 was examined for dual-mode hyperthermal therapy involving NIR laser and AMF. The MTT assay results demonstrate enhanced hyperthermia effects, validating the combined application of NIR laser and AMF as an effective modality for hyperthermia-induced tumor cell killing in vitro. The cell viability incubated with MZFC-4 was 10.3% when exposed to both 808 nm laser and AMF irradiation for 10 min, indicating that the combined PTT and MHT remarkably augmented the cytotoxicity of MZFC-4. The proof-of-concept in vitro demonstration indicates that the synthesized MZFC-4 is a promising nanomaterial as a targeted nanoheating agent for magneto-photothermal hyperthermia applications.

■ ASSOCIATED CONTENT

SI Supporting Information

The Supporting Information is available free of charge at <https://pubs.acs.org/doi/10.1021/acsnm.3c01929>.

Experimental materials; in vitro cell culture and incubated conditions; SEM; FT-IR spectra; DLS; magnetic properties as prepared samples; synthesis of the gel phantoms; schematic diagram of the magneto-photothermal experiment; heating curves and infrared thermal images of MZFC-*n*; and photothermal conversion efficiency (PDF)

■ AUTHOR INFORMATION

Corresponding Authors

Yunfei Yan – Key Laboratory of Low-grade Energy Utilization Technologies and Systems, Chongqing University, Chongqing 400044, China; orcid.org/0000-0002-2601-756X; Email: yunfeiyang@cqu.edu.cn

Lixian Li – Department of Pharmacy, Chongqing University Cancer Hospital, Chongqing 400030, China; Email: lilixian@cqu.edu.cn

Wen Siang Lew – School of Physical and Mathematical Sciences, Nanyang Technological University, Singapore 637371, Singapore; orcid.org/0000-0002-5161-741X; Email: wensiang@ntu.edu.sg

Authors

Kaiming Shen – Key Laboratory of Low-grade Energy Utilization Technologies and Systems, Chongqing University, Chongqing 400044, China; Department of Pharmacy, Chongqing University Cancer Hospital, Chongqing 400030, China; School of Physical and Mathematical Sciences, Nanyang Technological University, Singapore 637371, Singapore

Zongguo Xue – Key Laboratory of Low-grade Energy Utilization Technologies and Systems, Chongqing University, Chongqing 400044, China; Department of Pharmacy, Chongqing University Cancer Hospital, Chongqing 400030, China; School of Physical and Mathematical Sciences, Nanyang Technological University, Singapore 637371, Singapore

Shuo Wu – Key Laboratory of Low-grade Energy Utilization Technologies and Systems, Chongqing University, Chongqing 400044, China; Department of Pharmacy, Chongqing

University Cancer Hospital, Chongqing 400030, China; School of Physical and Mathematical Sciences, Nanyang Technological University, Singapore 637371, Singapore

Jingxiang You – Key Laboratory of Low-grade Energy Utilization Technologies and Systems, Chongqing University, Chongqing 400044, China; Department of Pharmacy, Chongqing University Cancer Hospital, Chongqing 400030, China; School of Physical and Mathematical Sciences, Nanyang Technological University, Singapore 637371, Singapore

Complete contact information is available at: <https://pubs.acs.org/doi/10.1021/acsnm.3c01929>

Notes

The authors declare no competing financial interest.

■ ACKNOWLEDGMENTS

The authors gratefully acknowledge financial support from the Fundamental Research Funds for the Central Universities (2019CDYGYB022) and the Natural Science Foundation of Chongqing (cstc2021jcyj-msxmX0448).

■ REFERENCES

- (1) Arami, H.; Kananian, S.; Khalifehzadeh, L.; Patel, C. B.; Chang, E.; Tanabe, Y.; Zeng, Y.; Madsen, S. J.; Mandella, M. J.; Natarajan, A.; Peterson, E. E.; Sinclair, R.; Poon, A. S. Y.; Gambhir, S. S. Remotely controlled near-infrared-triggered photothermal treatment of brain tumours in freely behaving mice using gold nanostar's. *Nat. Nanotechnol.* **2022**, *17*, 1015–1022.
- (2) Chen, J.; Gong, M.; Fan, Y.; Feng, J.; Han, L.; Xin, H. L.; Cao, M.; Zhang, Q.; Zhang, D.; Lei, D.; Yin, Y. Collective Plasmon Coupling in Gold Nanoparticle Clusters for Highly Efficient Photothermal Therapy. *ACS Nano* **2022**, *16*, 910–920.
- (3) Liu, W.; Wang, Y.; Wang, Y.; Li, X.; Qi, K.; Wang, J.; Xu, H. Black Silver Nanocubes@Amino Acid-Encoded Highly Branched Gold Shells with Efficient Photothermal Conversion for Tumor Therapy. *ACS Appl. Mater. Interfaces* **2022**, *15*, 236–248.
- (4) Nasser, B.; Alizadeh, E.; Bani, F.; Davaran, S.; Akbarzadeh, A.; Rabiee, N.; Bahadori, A.; Ziaei, M.; Bagherzadeh, M.; Saeb, M. R.; Mozafari, M.; Hamblin, M. R. Nanomaterials for photothermal and photodynamic cancer therapy. *Appl. Phys. Rev.* **2022**, *9*, 011317.
- (5) Wang, G.; Li, B.; Wu, L. Near-infrared photothermally enhanced catalysis for benzene hydroxylation. *J. Mater. Chem. A* **2022**, *10*, 21884–21892.
- (6) Yang, N.; Kang, Y.; Cong, Y.; Wang, X.; Yao, C.; Wang, S.; Li, L. Controllable Gold Nanocluster-Emulsion Interface for Direct Cell Penetration and Photothermal Killing. *Adv. Mater.* **2022**, No. e2208349.
- (7) Zhang, M.; Chen, Y.; Li, D.; He, Z.; Wang, H.; Wu, A.; Fei, W.; Zheng, C.; Liu, E.; Huang, Y. Gold Nanocage-Based Photothermal Ablation Facilitates In Situ Vaccination for Melanoma Therapy. *ACS Appl. Mater. Interfaces* **2022**, *14*, 38550–38561.
- (8) Zhang, Y.; Guo, Z.; Zhu, H.; Xing, W.; Tao, P.; Shang, W.; Fu, B.; Song, C.; Hong, Y.; Dickey, M. D.; Deng, T. Synthesis of Liquid Gallium@Reduced Graphene Oxide Core-Shell Nanoparticles with Enhanced Photoacoustic and Photothermal Performance. *J. Am. Chem. Soc.* **2022**, *144*, 6779–6790.
- (9) Bertuit, E.; Benassai, E.; Meriguet, G.; Greneche, J. M.; Baptiste, B.; Neveu, S.; Wilhelm, C.; Abou-Hassan, A. Structure-Property-Function Relationships of Iron Oxide Multicore Nanoflowers in Magnetic Hyperthermia and Photothermia. *ACS Nano* **2021**, *16*, 271–284.
- (10) Gavilan, H.; Avugadda, S. K.; Fernandez-Cabada, T.; Soni, N.; Cassani, M.; Mai, B. T.; Chantrell, R.; Pellegrino, T. Magnetic nanoparticles and clusters for magnetic hyperthermia: optimizing

their heat performance and developing combinatorial therapies to tackle cancer. *Chem. Soc. Rev.* **2021**, *50*, 11614–11667.

(11) Mamiya, H.; Fukumoto, H.; Cuya Huaman, J. L.; Suzuki, K.; Miyamura, H.; Balachandran, J. Estimation of Magnetic Anisotropy of Individual Magnetite Nanoparticles for Magnetic Hyperthermia. *ACS Nano* **2020**, *14*, 8421–8432.

(12) Shaw, S. K.; Kailashiya, J.; Gangwar, A.; Alla, S. K.; Gupta, S. K.; Prajapat, C. L.; Meena, S. S.; Dash, D.; Maiti, P.; Prasad, N. K. γ -Fe₂O₃ nanoflowers as efficient magnetic hyperthermia and photothermal agent. *Appl. Surf. Sci.* **2021**, *560*, 150025.

(13) Soares, P. I. P.; Laia, C. A. T.; Carvalho, A.; Pereira, L. C. J.; Coutinho, J. T.; Ferreira, I. M. M.; Novo, C. M. M.; Borges, J. P. Iron oxide nanoparticles stabilized with a bilayer of oleic acid for magnetic hyperthermia and MRI applications. *Appl. Surf. Sci.* **2016**, *383*, 240–247.

(14) Niraula, G.; Coaquira, J. A. H.; Zoppellaro, G.; Villar, B. M. G.; Garcia, F.; Bakuzis, A. F.; Longo, J. P. F.; Rodrigues, M. C.; Muraca, D.; Ayes, A. I.; Sinfrônio, F. S. M.; de Menezes, A. S.; Goya, G. F.; Sharma, S. K.; Sharma, S. K. Engineering Shape Anisotropy of Fe₃O₄- γ -Fe₂O₃ Hollow Nanoparticles for Magnetic Hyperthermia. *ACS Appl. Nano Mater.* **2021**, *4*, 3148–3158.

(15) Curcio, A.; Silva, A. K. A.; Cabana, S.; Espinosa, A.; Baptiste, B.; Menguy, N.; Wilhelm, C.; Abou-Hassan, A. Iron Oxide Nanoflowers @ CuS Hybrids for Cancer Tri-Therapy: Interplay of Photothermal Therapy, Magnetic Hyperthermia and Photodynamic Therapy. *Theranostics* **2019**, *9*, 1288–1302.

(16) Rincon-Iglesias, M.; Rodrigo, I.; B Berganza, L.; Serea, E. S. A.; Plazaola, F.; Lanceros-Mendez, S.; Lizundia, E.; Reguera, J. Core-Shell Fe₃O₄@Au Nanorod-Loaded Gels for Tunable and Anisotropic Magneto- and Photothermal. *Appl. Mater. Interfaces* **2022**, *14*, 7130–7140.

(17) Song, G.; Kenney, M.; Chen, Y. S.; Zheng, X.; Deng, Y.; Chen, Z.; Wang, S. X.; Gambhir, S. S.; Dai, H.; Rao, J. Carbon-coated FeCo nanoparticles as sensitive magnetic-particle-imaging tracers with photothermal and magnetothermal properties. *Nat. Biomed. Eng.* **2020**, *4*, 325–334.

(18) Sharma, S. K.; Shrivastava, N.; Rossi, F.; Tung, L. D.; Thanh, N. T. K. Nanoparticles-based magnetic and photo induced hyperthermia for cancer treatment. *Nano Today* **2019**, *29*, 100795.

(19) Park, Y.; Demessie, A. A.; Luo, A.; Taratula, O. R.; Moses, A. S.; Do, P.; Campos, L.; Jahangiri, Y.; Wyatt, C. R.; Albarqi, H. A.; Farsad, K.; Slayden, O. D.; Taratula, O. Targeted Nanoparticles with High Heating Efficiency for the Treatment of Endometriosis with Systemically Delivered Magnetic Hyperthermia. *Small* **2022**, *18*, 2107808.

(20) Kang, M. A.; Fang, J.; Paragodaarachchi, A.; Kodama, K.; Yakobashvili, D.; Ichiyanagi, Y.; Matsui, H. Magnetically Induced Brownian Motion of Iron Oxide Nanocages in Alternating Magnetic Fields and Their Application for Efficient siRNA Delivery. *Nano Lett.* **2022**, *22*, 8852–8859.

(21) Garcia-Acevedo, P.; Gonzalez-Gomez, M. A.; Armosa-Prieto, A.; de Castro-Alves, L.; Pineiro, Y.; Rivas, J. Role of Dipolar Interactions on the Determination of the Effective Magnetic Anisotropy in Iron Oxide Nanoparticles. *Adv. Sci.* **2022**, *10*, 2203397.

(22) Rajan, A.; Sahu, N. K. Hydrophobic-to-Hydrophilic Transition of Fe₃O₄ Nanorods for Magnetically Induced Hyperthermia. *ACS Appl. Nano Mater.* **2021**, *4*, 4642–4653.

(23) Cui, D.; Han, L.; Jiang, W.; Chen, L.; Niu, N. Ag_{2–3x}Bi_xS Quantum Dots as Single-Component Theranostic Agents for Second Near-Infrared Fluorescence Imaging-Guided Photothermal Therapy. *ACS Appl. Nano Mater.* **2023**, *6*, 1303–1314.

(24) Liu, L.; Zhang, H.; Peng, L.; Wang, D.; Zhang, Y.; Yan, B.; Xie, J.; Xing, S.; Peng, F.; Liu, X. A copper-metal organic framework enhances the photothermal and chemodynamic properties of polydopamine for melanoma therapy. *Acta Biomater.* **2023**, *158*, 660–672.

(25) Singh, B.; Bahadur, R.; Maske, P.; Gandhi, M.; Singh, D.; Srivastava, R. Preclinical safety assessment of red emissive gold nanocluster conjugated crumpled MXene nanosheets: a dynamic duo

for image-guided photothermal therapy. *Nanoscale* **2023**, *15*, 2932–2947.

(26) Vazquez-Prada, K. X.; Moonshi, S. S.; Wu, Y.; Akther, F.; Tse, B. W. C.; Sokolowski, K. A.; Peter, K.; Wang, X.; Xu, G.; Ta, H. T. A Spiky Silver-Iron Oxide Nanoparticle for Highly Efficient Targeted Photothermal Therapy and Multimodal Imaging of Thrombosis. *Small* **2023**, *19*, 2205744.

(27) Yin, B.; Ho, W. K. H.; Xia, X.; Chan, C. K. W.; Zhang, Q.; Ng, Y. M.; Lam, C. Y. K.; Cheung, J. C. W.; Wang, J.; Yang, M.; Wong, S. H. D. A Multilayered Mesoporous Gold Nanoarchitecture for Ultraeffective Near-Infrared Light-Controlled Chemo/Photothermal Therapy for Cancer Guided by SERS Imaging. *Small* **2023**, *19*, 2206762.

(28) Yu, X.; Yang, T.; Liu, R.; Wu, D.; Tian, D.; Zhou, T.; Yan, H.; He, S.; Zeng, H. Simultaneous Enhancement of Magnetothermal and Photothermal Responses by Zn, Co Co-Doped Ferrite Nanoparticles. *Small* **2022**, *18*, 2205037.

(29) Rajan, A.; Sahu, N. K. Review on magnetic nanoparticle-mediated hyperthermia for cancer therapy. *J. Nanopart. Res.* **2020**, *22*, 319.

(30) Rodrigues, H. F.; Capistrano, G.; Bakuzis, A. F. In vivo magnetic nanoparticle hyperthermia: a review on preclinical studies, low-field nano-heaters, noninvasive thermometry and computer simulations for treatment planning. *Int. J. Hyperthermia* **2020**, *37*, 76–99.

(31) Maier-Hauff, K.; Ulrich, F.; Nestler, D.; Niehoff, H.; Wust, P.; Thiesen, B.; Orawa, H.; Budach, V.; Jordan, A. Efficacy and safety of intratumoral thermotherapy using magnetic iron-oxide nanoparticles combined with external beam radiotherapy on patients with recurrent glioblastoma multiforme. *J. Neurooncol.* **2011**, *103*, 317–324.

(32) LeBrun, A.; Joglekar, T.; Bieberich, C.; Ma, R.; Zhu, L. Identification of infusion strategy for achieving repeatable nanoparticle distribution and quantification of thermal dosage using micro-CT Hounsfield unit in magnetic nanoparticle hyperthermia. *Int. J. Hyperthermia* **2016**, *32*, 132–143.

(33) Vassallo, M.; Martella, D.; Barrera, G.; Celegato, F.; Coisson, M.; Ferrero, R.; Olivetti, E. S.; Troia, A.; Sozeri, H.; Parmeggiani, C.; Wiersma, D. S.; Tiberto, P.; Manzin, A. Improvement of Hyperthermia Properties of Iron Oxide Nanoparticles by Surface Coating. *ACS Omega* **2023**, *8*, 2143–2154.

(34) Gresits, I.; Thuróczy, G.; Sági, O.; Homolya, I.; Bagaméry, G.; Jajári, D.; Babos, M.; Major, P.; Márkus, B. G.; Simon, F. A highly accurate determination of absorbed power during magnetic hyperthermia. *J. Phys. D: Appl. Phys.* **2019**, *52*, 375401.

(35) Wang, C.; Hsu, C. H.; Li, Z.; Hwang, L. P.; Lin, Y. C.; Chou, P. T.; Lin, Y. Y. Effective heating of magnetic nanoparticle aggregates for in vivo nano-theranostic hyperthermia. *Int. J. Nanomed.* **2017**, *12*, 6273–6287.

(36) Kim, J. W.; Wang, J.; Kim, H.; Bae, S. Concentration-dependent oscillation of specific loss power in magnetic nanofluid hyperthermia. *Sci. Rep.* **2021**, *11*, 733.

(37) Das, R.; Rinaldi-Montes, N.; Alonso, J.; Amghouz, Z.; Garaio, E.; Garcia, J. A.; Gorria, P.; Blanco, J. A.; Phan, M. H.; Srikanth, H. Boosted Hyperthermia Therapy by Combined AC Magnetic and Photothermal Exposures in Ag/Fe₃O₄ Nanoflowers. *Appl. Mater. Interfaces* **2016**, *8*, 25162–25169.

(38) Tang, P.; Liu, Y.; Liu, Y.; Meng, H.; Liu, Z.; Li, K.; Wu, D. Thermochromism-induced temperature self-regulation and alternating photothermal nanohelix clusters for synergistic tumor chemo/photothermal therapy. *Biomaterials* **2019**, *188*, 12–23.

(39) Zhu, X. M.; Wan, H. Y.; Jia, H.; Liu, L.; Wang, J. Porous Pt Nanoparticles with High Near-Infrared Photothermal Conversion Efficiencies for Photothermal Therapy. *Adv. Healthc. Mater.* **2016**, *5*, 3165–3172.

(40) Zhang, X.; Xi, Z.; Machuki, J. O.; Luo, J.; Yang, D.; Li, J.; Cai, W.; Yang, Y.; Zhang, L.; Tian, J.; Guo, K.; Yu, Y.; Gao, F. Gold Cube-in-Cube Based Oxygen Nanogenerator: A Theranostic Nanoplatfor-

Phototherapy and Multimodal Imaging. *ACS Nano* **2019**, *13*, 5306–5325.

(41) Jiang, S.; Zhu, F.; Lin, Y.; Ran, L.; Lin, F.; Tian, H.; Hu, T.; Wang, P.; Lu, C. Photothermal-augmented reactive oxygen species oxidative synergistic therapy based on nanoceria doped mesoporous polydopamine nanoplatteform. *Mater. Des.* **2023**, *225*, 111590.

(42) Khuyen, H. T.; Huong, T. T.; Van, N. D.; Huong, N. T.; Vu, N.; Lien, P. T.; Nam, P. H.; Nghia, V. X. Synthesis of Multifunctional Eu(III) Complex Doped Fe₃O₄/Au Nanocomposite for Dual Photo-Magnetic Hyperthermia and Fluorescence Bioimaging. *Molecules* **2023**, *28*, 749.

(43) Shabalkin, I. D.; Komlev, A. S.; Tsymbal, S. A.; Burmistrov, O. I.; Zverev, V. I.; Krivoschapkin, P. V. Multifunctional tunable ZnFe₂O₄@MnFe₂O₄ nanoparticles for dual-mode MRI and combined magnetic hyperthermia with radiotherapy treatment. *J. Mater. Chem. B* **2023**, *11*, 1068–1078.

(44) Fernández-Afonso, Y.; Asín, L.; Beola, L.; Fratila, R. M.; Gutiérrez, L. Influence of Magnetic Nanoparticle Degradation in the Frame of Magnetic Hyperthermia and Photothermal Treatments. *ACS Appl. Nano Mater.* **2022**, *5*, 16220–16230.

(45) Balachandran, Y. L.; Wang, W.; Yang, H.; Tong, H.; Wang, L.; Liu, F.; Chen, H.; Zhong, K.; Liu, Y.; Jiang, X. Heterogeneous Iron Oxide/Dysprosium Oxide Nanoparticles Target Liver for Precise Magnetic Resonance Imaging of Liver Fibrosis. *ACS Nano* **2022**, *16*, 5647–5659.

(46) Segers, F. M. E.; Ruder, A. V.; Westra, M. M.; Lammers, T.; Dadfar, S. M.; Roemhild, K.; Lam, T. S.; Kooi, M. E.; Cleutjens, K.; Verheyen, F. K.; Schurink, G. W. H.; Haenen, G. R.; van Berkel, T. J. C.; Bot, I.; Halvorsen, B.; Sluimer, J. C.; Biessen, E. A. L. Magnetic resonance imaging contrast-enhancement with superparamagnetic iron oxide nanoparticles amplifies macrophage foam cell apoptosis in human and murine atherosclerosis. *Cardiovasc. Res.* **2022**, *118*, 3346–3359.

(47) Espinosa, A.; Kolosnjaj-Tabi, J.; Abou-Hassan, A.; Plan Sangnier, A.; Curcio, A.; Silva, A. K. A.; Di Corato, R.; Neveu, S.; Pellegrino, T.; Liz-Marzán, L. M.; Wilhelm, C. Magnetic (Hyper)Thermia or Photothermia? Progressive Comparison of Iron Oxide and Gold Nanoparticles Heating in Water, in Cells, and In Vivo. *Adv. Funct. Mater.* **2018**, *28*, 1803660.

(48) Yao, X.; Niu, X.; Ma, K.; Huang, P.; Grothe, J.; Kaskel, S.; Zhu, Y. Graphene Quantum Dots-Capped Magnetic Mesoporous Silica Nanoparticles as a Multifunctional Platform for Controlled Drug Delivery, Magnetic Hyperthermia, and Photothermal Therapy. *Small* **2017**, *13*, 1602225.

(49) Fiorito, S.; Soni, N.; Silvestri, N.; Brescia, R.; Gavilan, H.; Conteh, J. S.; Mai, B. T.; Pellegrino, T. Fe₃O₄@Au@Cu_{2-x}S Heterostructures Designed for Tri-Modal Therapy: Photo-Magnetic Hyperthermia and (64) Cu Radio-Insertion. *Small* **2022**, *18*, 2200174.

(50) Xie, J.; Yan, C.; Yan, Y.; Chen, L.; Song, L.; Zang, F.; An, Y.; Teng, G.; Gu, N.; Zhang, Y. Multi-modal Mn-Zn ferrite nanocrystals for magnetically-induced cancer targeted hyperthermia: a comparison of passive and active targeting effects. *Nanoscale* **2016**, *8*, 16902–16915.

(51) Jadhav, S. V.; Kim, B. M.; Lee, H. Y.; Im, I. C.; Rokade, A. A.; Park, S. S.; Patil, M. P.; Kim, G. D.; Yu, Y. S.; Lee, S. H. Induction heating and in vitro cytotoxicity studies of MnZnFe₂O₄ nanoparticles for self-controlled magnetic particle hyperthermia. *J. Alloys Compd.* **2018**, *745*, 282–291.

(52) Kaur, N.; Chudasama, B. Tunable Curie temperature of Mn_{0.6}Zn_{0.4}Fe₂O₄ nanoparticles. *J. Magn. Magn. Mater.* **2018**, *465*, 164–168.

(53) Kondo, T.; Mori, K.; Hachisu, M.; Yamazaki, T.; Okamoto, D.; Watanabe, M.; Gonda, K.; Tada, H.; Hamada, Y.; Takano, M.; Ohuchi, N.; Ichiyangi, Y. Alternating current magnetic susceptibility and heat dissipation by Mn_{1-x}Zn_xFe₂O₄ nanoparticles for hyperthermia treatment. *J. Appl. Phys.* **2015**, *117*, 17D157.

(54) Vinícius-Araújo, M.; Shrivastava, N.; Sousa-Junior, A. A.; Mendanha, S. A.; Santana, R. C. D.; Bakuzis, A. F. Zn_xMn_{1-x}Fe₂O₄@

SiO₂:zNd³⁺ Core-Shell Nanoparticles for Low-Field Magnetic Hyperthermia and Enhanced Photothermal Therapy with the Potential for Nanothermometry. *ACS Appl. Nano Mater.* **2021**, *4*, 2190–2210.

(55) Wang, H.; Wu, L.; Xu, L.; Zheng, L.; Wu, Y.; Wu, K.; Wang, J.; Chen, Q. Synthetic Multiscale Graphene Aerogel Polymer Composites with High-Conductive Performances for Hyperthermia Equipment. *Adv. Eng. Mater.* **2021**, *23*, 2001429.

(56) Eivazzadeh-Keihan, R.; Asgharnasl, S.; Moghim Aliabadi, H. A.; Tahmasebi, B.; Radinekiyan, F.; Maleki, A.; Bahreinizad, H.; Mahdavi, M.; Alavijeh, M. S.; Saber, R.; Lanceros-Mendez, S.; Shalan, A. E. Magnetic graphene oxide-lignin nanobiocomposite: a novel, eco-friendly and stable nanostructure suitable for hyperthermia in cancer therapy. *RSC Adv.* **2022**, *12*, 3593–3601.

(57) Zuo, X.; Wu, C.; Zhang, W.; Gao, W. Magnetic carbon nanotubes for self-regulating temperature hyperthermia. *RSC Adv.* **2018**, *8*, 11997–12003.

(58) Karimzadeh, S.; Safaei, B.; Jen, T.-C. Theoretical investigation of adsorption mechanism of doxorubicin anticancer drug on the pristine and functionalized single-walled carbon nanotube surface as a drug delivery vehicle: A DFT study. *J. Mol. Liq.* **2021**, *322*, 114890.

(59) Shen, S.; Feng, L.; Qi, S.; Cao, J.; Ge, Y.; Wu, L.; Wang, S. Reversible Thermochromic Nanoparticles Composed of a Eutectic Mixture for Temperature-Controlled Photothermal Therapy. *Nano Lett.* **2020**, *20*, 2137–2143.

(60) Kim, H. J.; Hyun, S. W.; Kim, S. H.; Choi, H. Mn-Zn ferrite nanoparticles for application in magnetic hyperthermia. *J. Radioanal. Nucl. Chem.* **2021**, *330*, 445–454.

(61) Mallesh, S.; Mondal, P.; Kavita, S.; Srinivas, V.; Nam, Y.-W. Effect of Ni substitution and annealing temperature on structural and magnetic properties of MnZn-Ferrites: Cytotoxicity study of ZnO and SiO₂ coated core shell structures. *Appl. Surf. Sci.* **2022**, *605*, 154648.

(62) Taufiq, A.; Bahtiar, S.; Saputro, R. E.; Yuliantika, D.; Hidayat, A.; Sunaryono, S.; Hidayat, N.; Samian, S.; Soontaranon, S. Fabrication of Mn_{1-x}Zn_xFe₂O₄ ferrofluids from natural sand for magnetic sensors and radar absorbing materials. *Heliyon* **2020**, *6*, 04577.

(63) Chen, H.; Shao, L.; Ming, T.; Sun, Z.; Zhao, C.; Yang, B.; Wang, J. Understanding the photothermal conversion efficiency of gold nanocrystals. *Small* **2010**, *6*, 2272–2280.

(64) Shen, K.; Yan, Y.; Gao, W.; Li, H.; Chen, W.; He, Z.; Li, L. Heat-Generating Mn_{0.5}Zn_{0.5}Fe₂O₄/MWCNTs nanocomposites for enhancing hyperthermia efficacy in magnetic hyperthermia applications. *J. Alloys Compd.* **2022**, *926*, 166806.